Comput. Methods Appl. Mech. Engrg. 260 (2013) 40–49

Contents lists available at SciVerse ScienceDirect

Comput. Methods Appl. Mech. Engrg.

journal homepage: www.elsevier.com/locate/cma

Electromechanical instability on dielectric polymer surface: Modeling and experiment

Harold S. Park [a,*], Qiming Wang [b], Xuanhe Zhao [b], Patrick A. Klein [c]

[a] Department of Mechanical Engineering, Boston University, Boston, MA 02215, United States
[b] Soft Active Materials Laboratory, Department of Mechanical Engineering and Materials Science, Duke University, Durham, NC 27708, United States
[c] Franklin Templeton Investments, San Mateo, CA 94403, United States

ARTICLE INFO

Article history:
Received 30 November 2012
Received in revised form 26 March 2013
Accepted 28 March 2013
Available online 6 April 2013

Keywords:
Locking
Finite element
Q1P0
Dielectric elastomer
Creasing
Cratering

ABSTRACT

We present a dynamic finite element formulation for dielectric elastomers that significantly alleviates the problem of volumetric locking that occurs due to the incompressible nature of the elastomers. We accomplish this by modifying the Q1P0 formulation of Simo et al. [1], and adapting it to the electromechanical coupling that occurs in dielectric elastomers. We demonstrate that volumetric locking has a significant impact on the critical electric fields that are necessary to induce electromechanical instabilities such as creasing and cratering in dielectric elastomers, and that the locking effects are most severe in problems related to recent experiments that involve significant constraints upon the deformation of the elastomers. We then compare the results using the new Q1P0 formulation to that obtained using standard 8-node linear and 27-node quadratic hexahedral elements to demonstrate the capability of the proposed approach. Finally, direct comparison to the recent experimental work on the creasing instability on dielectric polymer surface by Wang et al. [2] is presented. The present formulation demonstrates good agreement to experiment for not only the critical electric field for the onset of the creasing instability, but also the experimentally observed average spacing between the creases.

1. Introduction

Dielectric elastomers (DEs) are a class of soft, active materials that have attracted significant attention in recent years [3–8]. They have been found to provide excellent overall performance in actuation-based applications, including high specific elastic energy density, good efficiency and high speed of response. Furthermore, DEs are typically lightweight, flexible and inexpensive materials which makes them ideal candidates for high performance, low cost applications where fabrication of the DEs into a wide range of shapes and structures can easily be realized [9].

While DEs have been found to exhibit good performance with respect to a variety of actuation-relevant properties, including strain, actuation pressure, efficiency, response speed, and density [10], the key source of the technological excitement surrounding DEs stems from the fact that, if sandwiched between two compliant electrodes that apply voltage to the elastomer, the DE can exhibit both significant thinning and in-plane expansion. This unique large deformation-based actuation capability has led to many interesting applications for DEs, including the potential to harvest energy from sources as diverse as human muscle motion and ocean waves, medical devices, and perhaps most importantly, artificial muscles [3,4,7]. Furthermore, recent experimental studies by Wang et al. [11] and Shivapooja et al. [12] have exploited the large deformation and surface instabilities studied in DEs in the present work to generate dynamic surface patterns, and antifouling coatings, respectively. In both of these cases, it is the large deformation and instability of the polymer that enables the novel applications, which may not be achieved with traditional electroactive materials. In addition, the voltage required to deform the polymer scales with the thickness of the polymer, which therefore may not be very high for thin polymer films.

Due to these and other potentially groundbreaking applications, starting about 15 years ago with the seminal work of Pelrine et al. [10,13], there have been many experimental studies to elucidate the electromechanical behavior and properties of DEs [14–25].

Along with the experimental studies, many analytic theories that explain various aspects of the electromechanical behavior and properties of DEs have recently been developed [26–33,20,21]. Many of these theories have as their basis the original works in electro-elasticity, for example that of Maugin [34]. Furthermore, there have recently appeared a range of analytical studies on the stability and instability phenomena both in DEs [35–38], and other magneto-elastic materials [39].

While these analytic theories have led to many key insights regarding the electromechanical behavior and instabilities of DEs, it has been difficult to use these analytic theories to study the

* Corresponding author.
E-mail address: parkhs@bu.edu (H.S. Park).

0045-7825/$ - see front matter © 2013 Elsevier B.V. All rights reserved.
http://dx.doi.org/10.1016/j.cma.2013.03.020

inhomogeneous deformation and failure mechanisms, i.e. wrinkling [19,21], electromechanical snap-through instability [13], and more recently creasing and cratering instabilities [2,40,11] that have been observed experimentally.

Because of this, several papers have recently appeared proposing finite element (FEM) formulations for DEs [41–44,33,45–49]. The approaches of Zhao and Suo [41] and O'Brien et al. [44] are similar in that neither formulation accounted for the full electromechanical coupling, i.e. electrostatic effects were accounted for via inclusion in the mechanical free energy, while no electrostatic governing equation was solved. The approaches of Vu et al. [42] and Zhou et al. [43] are similar in that both utilized finite deformation, fully coupled electromechanical equations that were solved neglecting inertia. While the work of Vu et al. [42] did not consider electromechanical instabilities, such effects were considered by Zhou et al. [43], though difficulties in tracking the entire history of the electromechanical instability were found due to the static formulation. Wissler and Mazza [45] solved the coupled electromechanical problem using Poisson's equation for the electrostatics, though again, electromechanical instabilities were not considered. Recently, Park and Nguyen [46] and also Khan et al. [47] proposed viscoelastic FEM models for DEs.

Overall, there exist two major unresolved issues in the existing FEM modeling literature. First, none of the previous approaches have demonstrated the ability to capture inhomogeneous deformation and failure modes (creasing, cratering, snap-through, wrinkling) that result from the electromechanical instability within a large deformation framework. Second, none of the previous approaches has been able to resolve the electromechanical instabilities while ensuring that the incompressible nature of the material response, and thus avoidance of volumetric locking effects, is accounted for.

The first issue was resolved through a recent FEM formulation proposed by Park et al. [50], who utilized inertia to capture electromechanical instabilities that arise through the constitutive model and field equations of Suo et al. [26]. Inertia is important for this approach as quasistatic FEM techniques, without special techniques such as the arclength method, fail once the loss of ellipticity (corresponding to softening in the voltage-charge curve for DEs) occurs. In contrast, the use of inertia enables the simulation to continue into the electromechanical softening regime, as demonstrated by Park et al. [50] and Park and Nguyen [46]. The role of inertia in electromechanically coupled problems is thus exactly analogous to its role in single field mechanical strain softening problems [51]. Using the dynamic formulation, they were able to demonstrate the basic electromechanical instabilities that occur in DEs under electrostatic loading, i.e. snap-through instabilities, surface wrinkling and creasing.

However, the work of Park et al. [50] did not resolve the second issue, i.e. that of volumetric locking that arises due to the incompressible material response of the DEs. As discussed by Belytschko et al. [52], FEM modeling of volumetric locking has a lengthy history, though the salient point is that the vast majority of the literature has been targeted towards single-field (i.e. mechanical-only) problems. In the present work, we extend one such approach to alleviating volumetric locking, the classic three-field Hu–Washizu Q1P0 formulation of Simo et al. [1], to problems involving coupling of the mechanical and electrostatic domains. We note that while the viscoelastic formulation of Park and Nguyen [46] also utilized the Q1P0 formulation of Simo et al. [1] to alleviate volumetric locking, an explicit comparison to experimental results to demonstrate the necessity and accuracy of the electromechanical Q1P0 formulation was not performed. Because of this, we also demonstrate the capability of the proposed approach in accurately capturing the experimentally observed critical electric fields needed to induce electromechanical instabilities, as well as the experimentally observed spacing by Wang et al. [2]. Comparisons are also made to standard three-dimensional linear and quadratic hexahedral FEs to demonstrate the utility of a specialized formulation to alleviate volumetric locking effects.

2. Background: nonlinear electromechanical field theory

The numerical results we present in this work are obtained using a FEM discretization of the electromechanical field theory recently proposed by Suo et al.[26], and recently reviewed by Suo [27]. In this field theory, at mechanical equilibrium, the nominal stress s_{iJ} satisfies the following (weak) equation:

$$\int_V s_{iJ}\frac{\partial \xi_i}{\partial X_J}dV = \int_V \left(B_i - \rho\frac{\partial^2 x_i}{\partial t^2}\right)\xi_i dV + \int_A T_i\xi_i dA, \tag{1}$$

where ξ_i is an arbitrary vector test function, B_i is the body force per unit reference volume V, ρ is the mass density of the material and T_i is the force per unit area that is applied on the surface A in the reference configuration.

For the electrostatic problem, the nominal electric displacement $\tilde{D}_I$ satisfies the following (weak) equation:

$$-\int_V \tilde{D}_I\frac{\partial \eta}{\partial X_I}dV = \int_V q\eta dV + \int_A \omega\eta dA, \tag{2}$$

where η is an arbitrary scalar test function, q is the volumetric charge density and ω is the surface charge density, both with respect to the reference configuration.

We make several relevant comments with regards to the field equations in (1) and (2). First, if the vector test function ξ_i is chosen to represent a virtual displacement δu_i, the mechanical weak form in (1) represents the well-known statement of virtual mechanical work, where the nominal stress S_{iJ} is work conjugate to the gradient of virtual displacement δu_i. Second, if the electrical test function η in (2) is chosen to be the virtual potential $\delta\phi$, then the electrostatic weak form in (2) can also be interpreted within a virtual work context, where the nominal electric displacement $\tilde{D}_I$ is work conjugate to the gradient of virtual potential $\delta\phi$. Third, the strong form of the mechanical weak form in (1) is the well-known momentum equation, while the strong form of the electrostatic weak form in (2) is the well-known Gauss's law.

Because we are solving an electromechanical boundary value problem, it is relevant to discuss the details of the boundary conditions for each field equation. Specifically, the electromechanical boundary conditions are in fact the standard boundary conditions for each of the single domain problems. Specifically, these are applied tractions and displacements for the mechanical domain and applied voltages and charges for the electrostatic domain. No non-standard boundary conditions are needed in the present formulation.

We also note that the weak formulations in (1) and (2) do not account for the possible effect of the surrounding free space. However, both for the problem we analyze in the current work, as well as the vast majority of experimental DE configurations, the DE is actuated by coating it with electrodes and the effect of electric fields around the edges of the electrodes is negligible. For other situations in which an air gap exists between one electrode and the polymer, it is likely that the electric field in the air will have a significant effect on the instability mechanism [53].

We note that the theory of Suo et al. [26] is not the only nonlinear electromechanical field theory that exists; earlier works by Dorfmann and Ogden [29,30] and McMeeking and Landis [31] also proposed nonlinear electromechanical field theories for deformable elastomeric materials. For this work, we utilize the governing nonlinear electromechanical field equations of Suo et al. [26] for the following five reasons: (1) The field variables (mechanical

force, electric potential) are both experimentally measurable quantities; (2) The theory circumvents the fact that the true electric field and true electric displacement are not work conjugate in a dielectric solid; (3) The theory circumvents the fact that the force between two electric charges in a dielectric solid is not a measurable quantity; (4) The resulting field equations are the standard mechanical momentum equation and the electrostatic Gauss's equation, which can be approximated using the FEM in a straightforward manner with standard boundary conditions; (5) As shown by Suo et al. [26], in the limiting case of a fluid dielectric, the theory recovers the Maxwell stress. A more detailed discussion regarding these issues can be found in the works of McMeeking and Landis [31] and Suo et al. [26]. Having made note of these notions, we move forward to the discussion of the resulting FEM formulation.

2.1. Constitutive model of an ideal dielectric elastomer

As the governing field equations in (1) and (2) are decoupled, the electromechanical coupling occurs through the material laws. The hyperelastic material law we will utilize in this paper has been utilized in the literature to study the nonlinear deformations of electrostatically actuated polymers, i.e. see the works of Vu et al. [42] and Zhao and suo [54], and has been shown to agree well with experimental results [55]. We do not account for dissipative mechanisms, i.e. viscoelasticity or current leakage [56], or thermal effects in the present work.

Due to the fact that the DE is a rubber-like polymer, phenomenological free energy expressions are typically used to model the deformation of the polymer chains; in the present work, we will utilize the form [42,54]

$$W(\mathbf{C},\tilde{\mathbf{E}}) = \mu W_0 - \frac{1}{2}\lambda(\ln J)^2 - 2\mu W_0'(I_1=3)\ln J - \frac{\epsilon}{2}JC_{IJ}^{-1}\tilde{E}_I\tilde{E}_J, \qquad (3)$$

where W_0 is the mechanical free energy density in the absence of an electric field, ϵ is the permittivity of the material, $J=\det(\mathbf{F})$, where $\mathbf{F}$ is the continuum deformation gradient, C_{IJ}^{-1} are the components of the inverse of the right Cauchy-Green tensor $\mathbf{C}$, λ is the bulk modulus, μ is the shear modulus and $\tilde{E}$ is the nominal electric field. The free energy in (3) has been termed the ideal dielectric elastomer by Zhao et al. [38] for reasons elaborated upon below.

We will model the mechanical behavior of the DE using the well-known [57] rubber hyperelastic function, where the mechanical free energy W_0 in (3) is written as

$$\frac{W_0(I_1)}{\mu} = \frac{1}{2}(I_1-3) + \frac{1}{20N}(I_1^2-9) + \frac{11}{1050N^2}(I_1^3-27) + \frac{19}{7000N^3}(I_1^4-81) + \frac{519}{673750N^4}(I_1^5-243), \qquad (4)$$

where N is a measure of the cross link density, I_1 is the trace of $\mathbf{C}$, and where the Arruda–Boyce model reduces to a Neo–Hookean model if $N\to\infty$. We emphasize that previous experimental studies of Wissler and Mazza [23] have shown that the Arruda–Boyce model performs very well in capturing the large deformation behavior of DEs. We also note that simpler hyperelastic models such as the Gent model may be used in place of the Arruda–Boyce model.

Physically, the equilibrium free energy W in (3) represents the fact that an elastomer is a three-dimensional network of long and flexible polymers, held together by crosslinks. Each polymer chain consists of a large number of monomers. Consequently, the crosslinks have negligible effect on the polarization of the monomers - that is, the elastomer can polarize nearly as freely as a polymer melt. As an idealization, we may assume that the dielectric behavior of an elastomer is exactly the same as that of a polymer melt.

Furthermore, in an elastomer, each individual polymer chain has a finite contour length. When the elastomer is subject to no loads, the polymer chains are coiled, allowing a large number of conformations. Subject to loads, the polymer chains become less coiled. As the loads increase, the end-to-end distance of each polymer chain approaches the finite contour length, and the elastomer approaches a limiting stretch. On approaching the limiting stretch, the elastomer stiffens steeply, which is captured by the Arruda-Boyce hyperelastic model in (4).

3. Finite element discretization

We now present the FEM discretization of the governing electromechanical field equations in (1) and (2); we note that this section presents in a slightly different form the formulation of Park et al. [50], but is given for completeness because the Q1P0 formulation that is the main result of this paper builds upon the earlier work.

The unknown FEM nodal degrees of freedom are the accelerations $\mathbf{a}$ in the mechanical domain, and the electric potential Φ in the electrostatic domain, where the nominal electric field $\tilde{\mathbf{E}} = -\frac{\partial\Phi(\mathbf{X},t)}{\partial\mathbf{X}}$. Both the mechanical displacement and the electric potential are discretized using standard FE shape functions, i.e.

$$x_i(\mathbf{X},t) - X_i = N_a(\mathbf{X})u_{ai}(t),$$
$$\Phi(\mathbf{X},t) = N_a(\mathbf{X})\Phi_a(t), \qquad (5)$$

while the test functions ξ and η in (1) and (2) are also interpolated using the same shape functions to ensure a Bubnov–Galerkin formulation.

Because our simulation is dynamic, and thus involves integration through time, and because the linearization of the governing equations results in a nonlinear system of equations to solve that involves iterations for each time step, we first define some important notation to avoid confusion in the section ahead. Specifically, we use the following notation that involves both superscripts and subscripts, i.e. $\mathbf{R}^n_{(i+1)}$. The subscript $(i+1)$ indicates the iteration count at time step n, which is the superscript.

Discretizing (1) and (2) using the FEM shape functions, the balance equations at time t^{n+1} can be written in residual form as

$$\mathbf{R}_m^{n+1} = \mathbf{f}_{m,ext}^{n+1} - (\mathbf{M}\mathbf{a}^{n+1} + \mathbf{f}_m^{n+1}), \qquad (6)$$
$$\mathbf{R}_e^{n+1} = \mathbf{f}_{e,ext}^{n+1} - \mathbf{f}_e^{n+1},$$
$$\mathbf{R}^{n+1} = \begin{pmatrix}\mathbf{R}_m^{n+1}\\ \mathbf{R}_e^{n+1}\end{pmatrix},$$

where

$$f_m^{n+1} = \int_V s_{ij}\frac{\partial N_a}{\partial X_J}dV, \qquad (7)$$
$$f_{m,ext}^{n+1} = \int_V B_i N_a dV + \int_A T_i N_a dA,$$
$$f_e^{n+1} = \int_V \tilde{D}_J\frac{\partial N_a}{\partial X_J}dV,$$
$$f_{e,ext}^{n+1} = \int_V qN_a dV + \int_A \omega N_a dA,$$

where $\mathbf{R}_m^{n+1}$ is the mechanical residual at time $n+1$, $\mathbf{R}_e^{n+1}$ is the electrostatic residual, $\mathbf{f}_m^{n+1}$ and $\mathbf{f}_e^{n+1}$ are the internal mechanical and electrostatic forces, respectively, and $\mathbf{f}_{m,ext}^{n+1}$ and $\mathbf{f}_{e,ext}^{n+1}$ are the externally applied mechanical and electrostatic forces, respectively.

Because the mechanical problem is time-dependent due to the inertial terms, the mechanical displacements must be found from the acceleration using standard time-integration techniques. We utilize the Newmark implicit time integrator [58,52], which is unconditionally stable if the time integrator parameters are set

to $\beta = 1/4$ and $\gamma = 1/2$. Choosing these parameters in conjunction with the Newmark integrator leads to the following predicted displacements, velocities and accelerations based upon the well-known average acceleration, or trapezoidal rule

$$\begin{aligned}\tilde{\mathbf{d}}^{n+1} &= \mathbf{d}^n + \Delta t\mathbf{v}^n + \Delta t^2\left(\frac{1}{2}-\beta\right)\mathbf{a}^n, \\ \tilde{\mathbf{v}}^{n+1} &= \mathbf{v}^n + \Delta t(1-\gamma)\mathbf{a}^n, \\ \tilde{\mathbf{a}}^{n+1} &= \mathbf{a}^n,\end{aligned} \tag{8}$$

where the tilde indicates the predicted value. The updated, or corrected values are then given as

$$\begin{aligned}\mathbf{d}^{n+1} &= \tilde{\mathbf{d}}^{n+1} + \beta\Delta t^2\mathbf{a}^{n+1}, \\ \mathbf{v}^{n+1} &= \tilde{\mathbf{v}}^{n+1} + \gamma\Delta t\mathbf{a}^{n+1}.\end{aligned} \tag{9}$$

From the corrected part of the time integration algorithm in (9), an important relationship that we utilize below in deriving the linearized FEM equations is

$$\frac{\partial \mathbf{d}^{n+1}}{\partial \mathbf{a}^{n+1}} = \beta\Delta t^2\mathbf{I}, \tag{10}$$

where $\mathbf{I}$ in (10) is an identity vector.

We now linearize the residual mechanical and electrostatic equations in (6) to obtain a Newton solution of the electromechanically coupled equations by using the standard Taylor expansion

$$\begin{aligned}\mathbf{R}_{(i+1)} &= \mathbf{R}_{(i)} + \frac{\partial \mathbf{R}}{\partial \mathbf{r}}\Delta\mathbf{r}, \\ \Delta\mathbf{r} &= \begin{pmatrix}\Delta\mathbf{a} \\ \Delta\Phi\end{pmatrix},\end{aligned} \tag{11}$$

where the subscript in parenthesis in (11), i.e. $(i+1)$ and (i), indicate iteration numbers and not time steps. We linearize the residual by taking the derivative $\frac{\partial \mathbf{R}}{\partial \mathbf{r}}$ to obtain

$$\begin{aligned}\frac{\partial \mathbf{R}_m}{\partial \mathbf{r}} &= \frac{\partial \mathbf{R}_{(i+1),m}}{\partial \mathbf{d}_{(i+1)}}\frac{\partial \mathbf{d}_{(i+1)}}{\partial \mathbf{a}_{(i+1)}}\Delta\mathbf{a}_{(i+1)} + \frac{\partial \mathbf{R}_{(i+1),m}}{\partial \Phi_{(i+1)}}\Delta\Phi_{(i+1)} + \mathbf{M}\Delta\mathbf{a}_{(i+1)}, \\ \frac{\partial \mathbf{R}_e}{\partial \mathbf{r}} &= \frac{\partial \mathbf{R}_{(i+1),e}}{\partial \mathbf{d}_{(i+1)}}\frac{\partial \mathbf{d}_{(i+1)}}{\partial \mathbf{a}_{(i+1)}} + \frac{\partial \mathbf{R}_{(i+1),e}}{\partial \Phi_{(i+1)}}\Delta\Phi_{(i+1)},\end{aligned} \tag{12}$$

where the notation in (12) implies that all quantities are calculated for each iteration $(i+1)$ that are needed to fully update the FEM nodal acceleration $\mathbf{a}$ and electric potential Φ from time step t^n to t^{n+1}. Plugging (10) into (12), we obtain

$$\begin{aligned}\frac{\partial \mathbf{R}}{\partial \mathbf{r}} &= \begin{pmatrix}\mathbf{M}+\beta\Delta t^2\mathbf{K}_{mm} & \mathbf{K}_{me} \\ \beta\Delta t^2\mathbf{K}_{em} & \mathbf{K}_{ee}\end{pmatrix}, \\ \mathbf{K}_{mm} &= \frac{\partial \mathbf{f}_{(i+1),m}}{\partial \mathbf{d}_{(i+1)}} = \int_V H_{ijkL}\frac{\partial N_a}{\partial X_J}\frac{\partial N_b}{\partial X_L}dV, \\ \mathbf{K}_{me} &= \frac{\partial \mathbf{f}_{(i+1)}}{\partial \Phi_{(i+1)}} = \mathbf{K}_{em}^T = \frac{\partial \mathbf{f}_{(i+1),e}}{\partial \mathbf{d}_{(i+1)}} = -\int_V e_{kJL}\frac{\partial N_a}{\partial X_J}\frac{\partial N_b}{\partial X_L}dV, \\ \mathbf{K}_{ee} &= \frac{\partial \mathbf{f}_{(i+1),e}}{\partial \Phi_{(i+1)}} = -\int_V \epsilon_{JL}\frac{\partial N_a}{\partial X_J}\frac{\partial N_b}{\partial X_L}dV, \\ H_{ijkL}(\mathbf{C},\tilde{\mathbf{E}}) &= 2\delta_{ik}\frac{\partial W(\mathbf{C},\tilde{\mathbf{E}})}{\partial C_{JL}} + 4F_{iM}F_{kN}\frac{\partial^2 W(\mathbf{C},\tilde{\mathbf{E}})}{\partial C_{JM}\partial C_{LN}}, \\ e_{ijL}(\mathbf{C},\tilde{\mathbf{E}}) &= -2F_{iM}\frac{\partial^2 W(\mathbf{C},\tilde{\mathbf{E}})}{\partial C_{JM}\partial \tilde{E}_L}, \\ \epsilon_{JL}(\mathbf{C},\tilde{\mathbf{E}}) &= -\frac{\partial^2 W(\mathbf{C},\tilde{\mathbf{E}})}{\partial \tilde{E}_J\partial \tilde{E}_L}.\end{aligned} \tag{13}$$

Explicit expressions for the mechanical (H_{ijkL}), electromechanical (e_{ijL}) and electrostatic (ϵ_{JL}) stiffnesses as derived from the coupled electromechanical free energy in (3) are given in Park et al. [50].

Because the solution of the residual in (11) requires that $\mathbf{R}_{(i+1)} = 0$, the increment of the FEM nodal acceleration $\Delta\mathbf{a}$ and electric potential $\Delta\Phi$ for each iteration can be obtained as

$$\begin{pmatrix}\Delta\mathbf{a}_{(i+1)} \\ \Delta\Phi_{(i+1)}\end{pmatrix} = \begin{pmatrix}\frac{\partial \mathbf{R}}{\partial \mathbf{u}}\end{pmatrix}^{-1}\begin{pmatrix}\mathbf{R}_{(i),m} \\ \mathbf{R}_{(i),e}\end{pmatrix}. \tag{14}$$

Convergence occurs when there is no further change in nodal acceleration $\Delta\mathbf{a}$ and potential $\Delta\Phi$. At that point, the prescribed mechanical or electrostatic loading is increased, and (14) is solved iteratively again until a new converged solution is obtained.

4. Q1P0 Formulation

4.1. Multiplicative split and constitutive equations

We now present the Q1P0 FEM formulation for DEs based on the approach of Simo et al. [1]. The Simo et al. work relies upon a three-field Hu–Washizu variation principle that treats the displacements, pressure and Jacobian as independent variables along with a kinematic split that decomposes the deformation gradient $\mathbf{F}$ into deviatoric and volumetric components.

We first introduce the relevant kinematic variables. Given a motion $\boldsymbol{\chi}(\mathbf{X},t)$, we can define the deformation gradient $\mathbf{F}$ and Jacobian J as

$$\begin{aligned}\mathbf{F} &= \frac{\partial \boldsymbol{\chi}}{\partial \mathbf{X}}, \\ J &= \det\mathbf{F}.\end{aligned} \tag{15}$$

We additionally define

$$\begin{aligned}\bar{\mathbf{F}} &= \Theta^{1/3}\hat{\mathbf{F}}, \\ \hat{\mathbf{F}} &= J^{-1/3}\mathbf{F}.\end{aligned} \tag{16}$$

where Θ is a new kinematic variable. The key idea underlying the multiplicative split of the deformation gradient into volumetric and deviatoric components is that while in the continuous case $\Theta(\mathbf{X},t) = J(\mathbf{X},t)$ such that $\bar{\mathbf{F}} = \mathbf{F}$, this identity does not hold when constructing a discrete, or finite-dimensional approximation. The modified right Cauchy–Green tensor $\mathbf{C}$ can now be written as

$$\begin{aligned}\mathbf{C} &= \mathbf{F}^T\mathbf{F}, \\ \hat{\mathbf{C}} &= J^{-2/3}\mathbf{C} = \hat{\mathbf{F}}^T\hat{\mathbf{F}},\end{aligned} \tag{17}$$

Due to the modification of the deformation gradient and Cauchy–Green tensors in (16) and (17), the free energy of the ideal DE in (3) is now written in the form

$$\begin{aligned}W &= \tilde{W}(\Theta^{2/3}\hat{\mathbf{C}},\tilde{\mathbf{E}}), \\ W &= \bar{W}(\Theta^{1/3}\hat{\mathbf{F}},\tilde{\mathbf{E}}).\end{aligned} \tag{18}$$

where we note that all resulting modifications to the free energy are to the mechanical kinematic variables, and not the nominal electric field. The corresponding first ($\mathbf{P}$) and second ($\mathbf{S}$) Piola–Kirchhoff stress tensors are then obtained via

$$\begin{aligned}\bar{\mathbf{S}} &= \left.\frac{\partial \tilde{W}(\mathbf{C},\tilde{\mathbf{E}})}{\partial \mathbf{C}}\right|_{\mathbf{C}=\Theta^{2/3}\hat{\mathbf{C}}}, \\ \bar{\mathbf{P}} &= \left.\frac{\partial \bar{W}(\mathbf{F},\tilde{\mathbf{E}})}{\partial \mathbf{F}}\right|_{\mathbf{F}=\Theta^{1/3}\hat{\mathbf{F}}}.\end{aligned} \tag{19}$$

4.2. Three-field Lagrangian and FEM equations

The modified kinematic variables are then utilized in the following Lagrangian:

$$L(\mathbf{d},\Theta,p)=\int_V \overline{W}(\Theta^{1/3}\hat{\mathbf{F}})dV+\int_V p(J-\Theta)dV+\Pi^{ext}(\mathbf{d})-K(\dot{\mathbf{d}}), \tag{20}$$

where $\Pi^{ext}(\mathbf{d})$ is the external work due to body forces and prescribed tractions, $K(\dot{\mathbf{d}})$ is the kinetic energy, and $\mathbf{d}$ is the FEM nodal displacements. It is clear that the purpose of the pressure p in (20) is to enforce the incompressibility condition in the discrete formulation, i.e. $J=\Theta$. Furthermore, as shown by Simo et al. [1], the pressure p is eliminated at the element level such that the resulting FEM equations include only the standard displacement (or acceleration) nodal degrees of freedom.

The Q1P0 nomenclature emerged because while the nodal displacement field is interpolated using standard, linear FEM shape functions, the element-level pressure and volume are approximated using a lower order, constant approximation. The Simo et al. [1] formulation also utilizes a projection approach, in which the shape function gradients $\mathbf{B}$ are decomposed into volumetric and deviatoric components, i.e.

$$\bar{\mathbf{B}}^I=\mathbf{B}^I_{dev}+\bar{\mathbf{B}}^I_{vol}, \tag{21}$$

where the explicit expressions for the $\bar{\mathbf{B}}$ shape function gradients can be found in Hughes [58], and where the volumetric component $\bar{\mathbf{B}}^I_{vol}$ in (21) is approximated by the mean dilation of the element which results in a lower order constant approximation for the volumetric deformation and pressure. We note that while $\mathbf{B}$ can also refer to the left Cauchy–Green deformation tensor, in the present work we use $\mathbf{B}$ to refer exclusively to FEM shape function gradients, as the left Cauchy–Green tensor is not utilized anywhere in this manuscript.

The resulting linearized, incremental FEM equations from the mixed projection approach were derived by Simo et al. [1], and take the form

$$\begin{aligned}&\mathbf{K}_{Q1P0}\Delta\mathbf{d}=-\mathbf{R},\\&\mathbf{K}_{Q1P0}=\mathbf{K}_{geo}+\mathbf{K}_{mat}+\mathbf{K}_p,\\&\mathbf{R}=\mathbf{f}^{ext}-\mathbf{f}^{int}-\mathbf{f}^{kin},\end{aligned} \tag{22}$$

where $\mathbf{K}_{geo}$ is the standard geometric contribution to the stiffness matrix, $\mathbf{K}_{mat}$ is the standard material contribution to the stiffness matrix, $\mathbf{K}_p$ is a non-standard contribution to the stiffness matrix that arises due to the presence of the new kinematic variable Θ in (20) [1,59], $\mathbf{f}^{ext}$ are external forces, $\mathbf{f}^{int}$ are internal forces, and $\mathbf{f}^{kin}$ are kinetic forces due to inertia. The modified shape functions $\bar{\mathbf{B}}$ are present in the internal force, i.e.

$$\mathbf{f}^{int}=\int_V(\bar{\mathbf{B}})^T\bar{\sigma}dv, \tag{23}$$

where $\bar{\sigma}$ is the Cauchy stress evaluated using the modified deformation gradient $\bar{\mathbf{F}}$ in (16), and the integral in (23) is evaluated in the current configuration dv. In the present work, we utilize the numerical finite different approach of Miehe [60] to calculate the stiffness matrix $\mathbf{K}_{Q1P0}$ in (22) based on the internal force in (23).

4.3. Q1P0 for electromechanical coupling

We now discuss the modification to the governing FEM equations in (13) that must occur to incorporate the mixed, projection-based Q1P0 approach. Specifically, there are three stiffness matrices that may be impacted, i.e. $\mathbf{K}_{mm},\mathbf{K}_{me}=\mathbf{K}^T_{em}$, and $\mathbf{K}_{ee}$. Of these three stiffnesses matrices, the electrical stiffness matrix $\mathbf{K}_{ee}$ is not impacted by the Q1P0 formulation because it is found purely by differentiation with respect to the nominal electric field $\tilde{\mathbf{E}}$. On the other hand, the mechanical stiffness matrix $\mathbf{K}_{mm}$ is exactly the Q1P0 stiffness matrix in (22), i.e.

$$\mathbf{K}_{mm}=\mathbf{K}_{Q1P0}=\mathbf{K}_{geo}+\mathbf{K}_{mat}+\mathbf{K}_p. \tag{24}$$

This leaves one stiffness matrix left to modify, the mixed electromechanical stiffness matrix $\mathbf{K}_{me}$. We derive this term by starting with the internal mechanical force, i.e.

$$\begin{aligned}&\mathbf{f}^{int}_m=\int_V\bar{\mathbf{B}}^T\bar{\sigma}dv,\\&\mathbf{f}^{int}_m=\int_V\bar{\mathbf{B}}^T\left(\frac{1}{J}\mathbf{F}\bar{\mathbf{S}}\mathbf{F}^T\right)dv|_{F=\Theta^{1/3}\hat{\mathbf{F}}},\end{aligned} \tag{25}$$

where we have converted the Cauchy stress $\bar{\sigma}$ to the second Piola–Kirchhoff stress $\bar{\mathbf{S}}$ in (25). The electromechanical stiffness is obtained via

$$\begin{aligned}&\mathbf{K}_{me}=\frac{\partial\mathbf{f}^{int}_m}{\partial\tilde{\mathbf{E}}}=\int_V\bar{\mathbf{B}}^T\left(\frac{1}{J}\mathbf{F}\frac{\partial\bar{\mathbf{S}}}{\partial\tilde{\mathbf{E}}}\mathbf{F}^T\right)\mathbf{B}dv|_{F=\Theta^{1/3}\hat{\mathbf{F}}},\\&\frac{\partial\bar{\mathbf{S}}}{\partial\tilde{\mathbf{E}}}=e_{ijL}(\mathbf{C},\tilde{\mathbf{E}})=-2F_{iM}\frac{\partial^2W(\mathbf{C},\tilde{\mathbf{E}})}{\partial C_{JM}\partial\tilde{E}_L}|_{C=\Theta^{2/3}\hat{\mathbf{C}}}.\end{aligned} \tag{26}$$

(25) makes clear that in extending the original Q1P0 formulation of Simo et al. [1] for the electromechanically coupled system of equations that describes DEs as derived by Park et al. [50], the major change (aside from the additional pressure-dependent stiffness contribution $\mathbf{K}_p$ for the purely mechanical problem) lies in the fact that the electromechanical stiffness matrices $\mathbf{K}_{me}=\mathbf{K}^T_{em}$ are mixed in the sense that the shape function gradient that comes from the mechanical domain is the projection gradient $\bar{\mathbf{B}}$, while the shape function gradient that comes from the electrostatic domain is the standard shape function gradient $\mathbf{B}$. This difference emerges because no modification to the electrostatic kinematic variables, i.e. the nominal electric field $\tilde{\mathbf{E}}$ or potential Φ is required to satisfy the incompressibility constraint, which occurs purely in the mechanical domain. The electrostatic force and stiffness are not modified except for the fact that the deformation gradient or stretch tensor that is used to evaluate them are done according to (16) and (17).

These modified stiffness matrices are then substituted into the previous governing FEM equations in (13), resulting in the new Q1P0 FEM formulation for DEs shown below:

$$\begin{pmatrix}\Delta\mathbf{a}_{(i+1)}\\ \Delta\Phi_{(i+1)}\end{pmatrix}=\left(\frac{\partial\mathbf{R}}{\partial\mathbf{r}}\right)^{-1}\begin{pmatrix}\mathbf{R}_{(i),m}\\ \mathbf{R}_{(i),e}\end{pmatrix}. \tag{27}$$

where

$$\frac{\partial\mathbf{R}}{\partial\mathbf{r}}=\begin{pmatrix}\mathbf{M}+\beta\Delta t^2\mathbf{K}_{Q1P0} & \mathbf{K}_{me}\\ \beta\Delta t^2\mathbf{K}_{em} & \mathbf{K}_{ee}\end{pmatrix}, \tag{28}$$

where the expression for $\mathbf{K}_{Q1P0}$ can be found in (24).

5. Numerical and Experimental Results

All numerical calculations were performed using the Sandia-developed simulation code Tahoe [61] using regular meshes of either 8-node linear hexahedral elements or 27-node quadratic hexahedral elements in 3D. The quadratic elements are utilized for comparison as it is well-known [52] that they are able to alleviate, though not eliminate, the effects of volumetric locking. A lumped mass matrix was used for all elements and calculations.

The problem we consider is motivated by the recent experimental results of Wang et al. [2,40,11], who attached a DE to a rigid substrate and subjected it to an increasing direct-current (DC) voltage. The voltage induced an electric field across the layer of the DE. Once the applied electric field in the DE reached a critical value, $\tilde{\mathbf{E}}_c=\sqrt{\mu/\epsilon}$, an electromechanical instability was observed, whereby the initially flat surface of the DE (Fig. (1a)) developed a pattern of creases (Fig. (1b)), followed by subsequent formation of deep

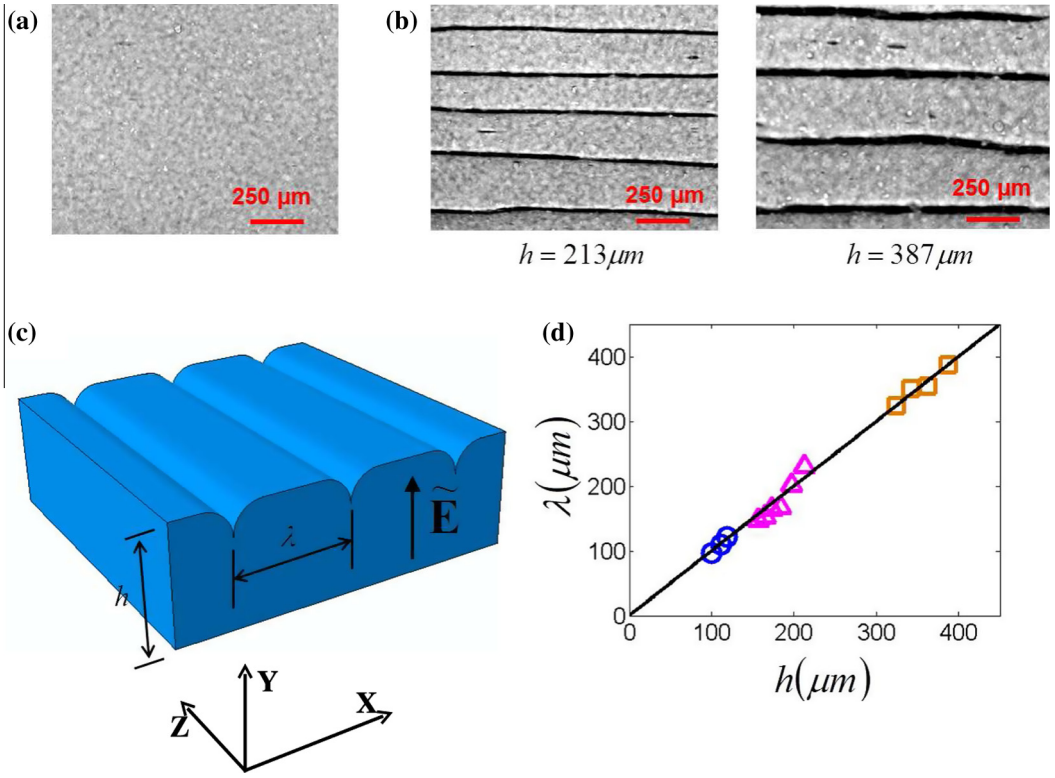

Fig. 1. Experimental results of electromechanical instability on the surface of a DE bonded on a rigid substrate: optical microscopic images of the DE at the (a) flat and (b) creased states, (c) schematic illustration of the aligned creases, and (d) the relation between the wavelength of the creases λ and the thickness of the DE film h.

craters from the initial creases. By pre-stretching the DE along one direction prior to bonding it on the substrate, Wang et al. [11] aligned the creases into parallel lines (Fig. (1c)). The average distance between adjacent creases λ was found to be approximately the same as the thickness of the pre-stretched film h, i.e. $\lambda \approx h$ (Fig. (1d)). It is important to note that this expression for the critical electric field, i.e. $\tilde{\mathbf{E}}_c = \sqrt{\mu/\epsilon}$ is specific to this particular creasing to cratering problem we consider here. For example, in a recent work, Wang et al. [62] showed that for bursting drops in a solid, the critical electric field appeared to follow the relationship $\tilde{\mathbf{E}}_c = 0.6\sqrt{\mu/\epsilon}$.

We modeled the experimental configuration of Wang et al. [2] by considering inhomogeneous deformation in a quasi-3D strip. The configuration is termed quasi-3D as all z-displacements are set to be zero to mimic a plane strain problem. To study this, we created a 3D strip with geometry $100 \times 4 \times 1$, which was discretized with 8-node hexahedral elements and 27-node hexahedral elements. For the 8-node hexahedral elements, mesh spacings of 1.0, 0.5, 0.25 and 0.125 were utilized to study convergence of the Q1P0 results for the critical electric field and the crease spacing. These mesh spacings resulted in 400, 1600, 6400 and 25,600 elements, respectively, and 1010, 3618, 13634 and 52,866 nodes, respectively. A study comparing the Q1P0, Hex8 and Hex27 elements was performed for the same mesh spacing of 1.0.

The enforced boundary conditions on the quasi-3D DE strip were as follows. The $-y$ surface of the DE was constrained in all three directions, while the $+x$ and $-x$ surfaces were also constrained in the x-direction to keep the length of the strip fixed. Electrostatic loading is applied using a monotonically increasing voltage on the $+y$ surface, which mimics the electrostatic loading condition in the experiments of Wang et al. [2]. Neglecting the regions around the edges of the electrodes, the deformation of the DE strip was homogeneous until electromechanical instability occurred. A problem schematic of the FEM model showing all mechanical and electrical boundary conditions is given in Fig. (2).

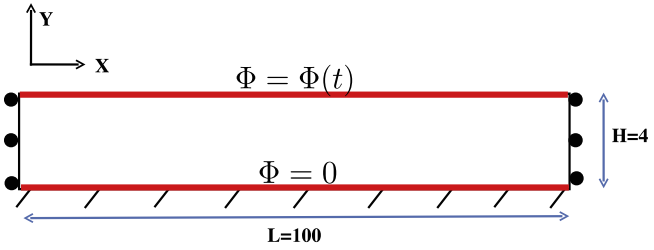

Fig. 2. Problem schematic showing length L and height H of the quasi-3D strip (thickness t is into the page), along with imposed mechanical and electrical boundary conditions. Note that the imposed voltage on the top surface $\Phi = \Phi(t)$ indicates that the voltage Φ is applied in a linear ramp format, starting from $\Phi = 0$ at $t = 0$.

We first show in Fig. (3) the evolution of the electromechanical instability as captured using the proposed Q1P0 FEM formulation, where the contours are of the displacement magnitude. Fig. (3a) shows the initial, random surface roughening that occurs once the critical electric field is reached. As the voltage is increased, Fig. (3b) shows the initial creases that form at the surface of the DE film. While the entire film is not shown, the surface creases form spontaneously all along the film surface from the initial random roughening. As the voltage is increased further, the initial surface creases evolve into craters as shown in Fig. (3c). The craters that form in the film can be quite deep; as shown in Fig. (3c), the magnitude of the mechanical displacement (_D_VEC) has a maximum value of about 3.5, the majority of which occurs in the vertical (thickness) direction of the film. Given that the film thickness is 4.0, it is clear that the deformation of the crease reaches a significant fraction of the film thickness, which eventually causes

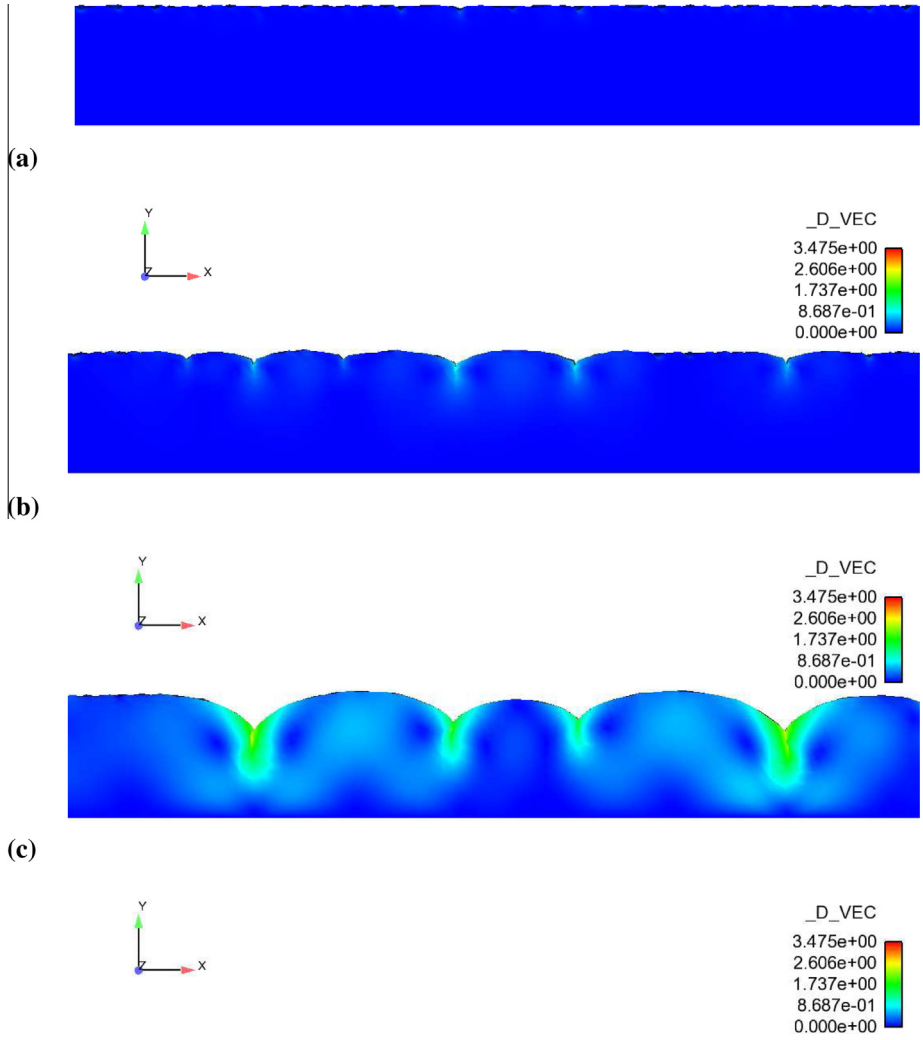

Fig. 3. Evolution of electromechanical instability on dielectric polymer surface from (a) initial surface roughening to (b) initiation of crease formation to (c) cratering using proposed Q1P0 FEM formulation. _D_VEC in the legend refers to the magnitude of the mechanical displacement. Note that the thickness of the film is 4.0.

numerical instability and failure of the simulation caused by non-convergence resulting from the extremely large material deformation.

We show a global comparison of the Q1P0, Hex8 and Hex27 results in Fig. (4). There are several noteworthy differences in the results. First, both the Hex27 and Q1P0 results in Figs. (4b) and (4c), respectively, indicate that both capture the initial surface creasing to cratering transition. In contrast, the cratering transition is not observed for the Hex8 element in Fig. (4a). Instead, upon formation of the initial surface creases, the creases are observed to propagate along the surface in response to the increasing voltage.

Because the creasing to cratering transition is not observed for the Hex8 element, we focus on the Q1P0 and Hex27 elements to compare the calculated distance (wavelength) between craters to the experimentally observed value of 1.5 times the film thickness. As seen in Fig. (4), for both the Hex27 and Q1P0 results that there is a distribution of distances (wavelengths) separating each crater. For the Hex27 result in Fig. (4b), total of 15 craters were identified, with the crater spacing ranging between 0.75 and 2.5 times the film thickness, with an average crater separation (wavelength) of about 1.48 times the film thickness. For the Q1P0 result in Fig. (4c), total of 19 craters were identified, with the crater spacing ranging between 0.94 and 1.88 times the film thickness, with an average crater separation (wavelength) of about 1.31 times the film thickness. Both the Q1P0 and Hex27 results for the crater separation show some difference as compared to the experimentally observed result of 1.0 times the film thickness, with the Q1P0 being more accurate. There are at least three possible reasons for this, with regards to the Q1P0 results. First, one possibility is that the length $L = 100$ of the quasi-3D strip is not large enough to remove any boundary effects; specifically, the length to thickness ratio in the FEM simulations is 25, whereas the experimental length to thickness ratio is larger than 1000. Second, as seen later in Fig. (6), for the finest mesh density we used of 0.125, the error in the critical electric field is still 10% as compared to the theoretical result. This suggests that a refinement in the mesh density may also lead to more accurate results in the crease spacing. Finally, the FEM model assumes an ideal dielectric law, which may be different from the polymer used in the experiments.

We next compare the performance of all elements in predicting the critical electric field to induce the surface creasing, i.e. the electromechanical instability. In looking at Fig. (5), it can be seen that in plotting the normalized voltage Φ versus the normalized charge Q that for all cases, there is an initial regime in which the voltage-charge curve is linear. However, there is eventually a sharp decrease in the slope, which indicates the onset of electromechanical instability. The electric field corresponding to this point is the one we use as the critical electric field $\tilde{\mathbf{E}}_c$. We compare the performance

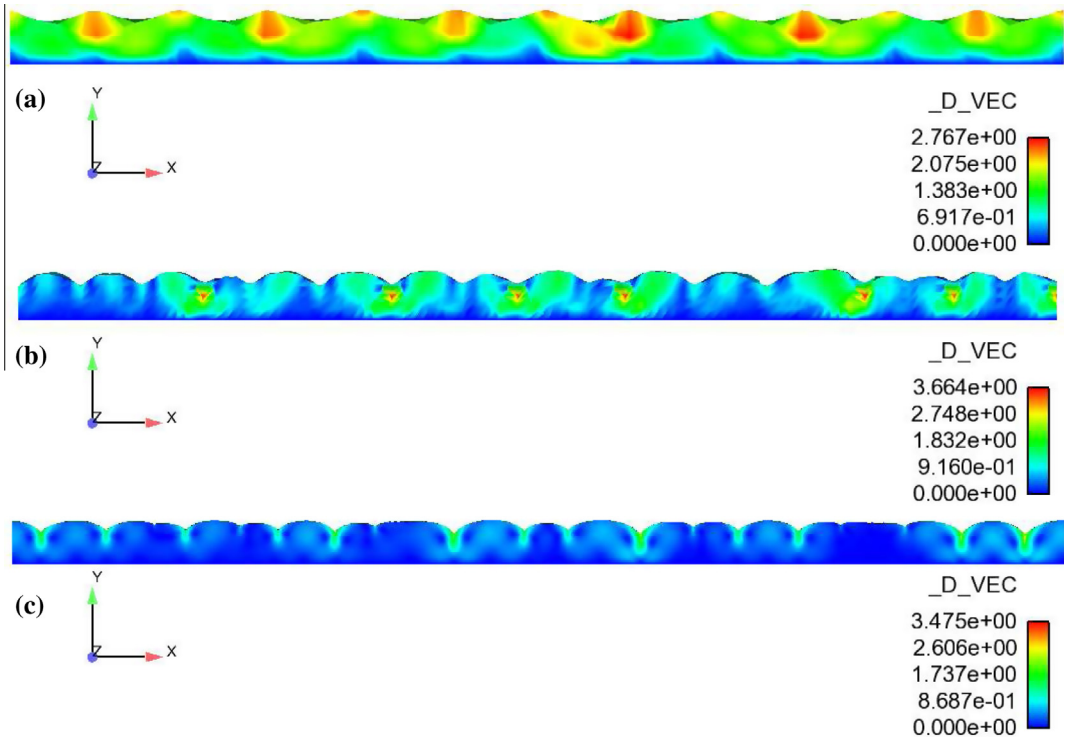

Fig. 4. Comparison of (a) Hex8, (b) Hex27, and (c) Q1P0 elements, all with mesh spacing of 1.0, for a representative configuration close to simulation failure. _D_VEC refers to the magnitude of the mechanical displacement. Note that the film thickness in all cases is 4.0.

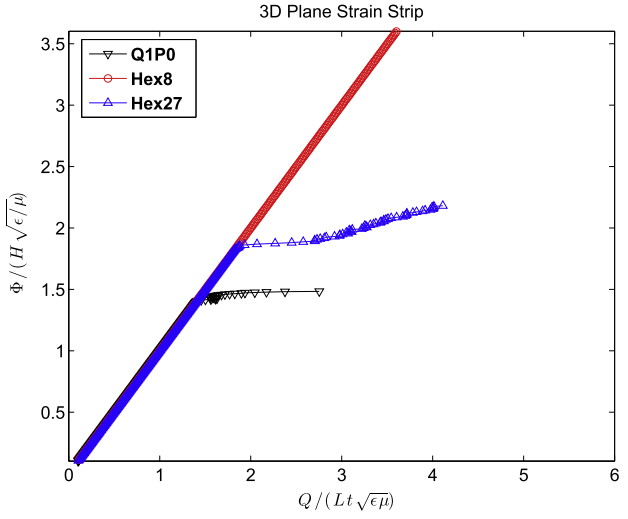

Fig. 5. Comparison of Q1P0, Hex8 and Hex27 elements for 3D plane strain strip, all with mesh spacing of 1.0. $H = 4$ is the height of the film, Q is the charge at the top surface of the film, $L = 100$ is the length of the film, $t = 1$ is the thickness of the film, $\epsilon = 1.0$ is the dielectric constant, Φ is the voltage, and $\mu = 1$ is the shear modulus.

of the Q1P0 formulation against the linear Hex8 and quadratic Hex27 elements for the same mesh size of 1.0, which is shown in Fig. (5). There, it is clear that the Hex8 element does not predict the electromechanical instability for normalized voltages that are more than 3.5 times the critical value of 1.0 [2]. In fact, the Hex8 element does not predict the instability until a normalized voltage of 5.2 is reached. The artificially large critical voltage for the Hex8 element occurs because it is well-known to be susceptible to volumetric locking effects, which means that it responds in an artificially stiff manner to applied forces, and thus a significantly larger voltage is needed to produce the electromechanical instability.

In contrast, the Hex27 element performs better; the critical normalized voltage is about 1.82, which is much lower than the Hex8 value, but much higher than the critical value of $\tilde{\mathbf{E}}_c = 1.0$ from theory and experiment ($\mu = \epsilon = 1$ in the FEM simulations). In contrast, the Q1P0 formulation predicts an $\tilde{\mathbf{E}}_c = 1.41$, which is substantially lower than the standard linear Hex8 and quadratic Hex27 elements but still about 40% higher than the experimentally reported value of 1.0.

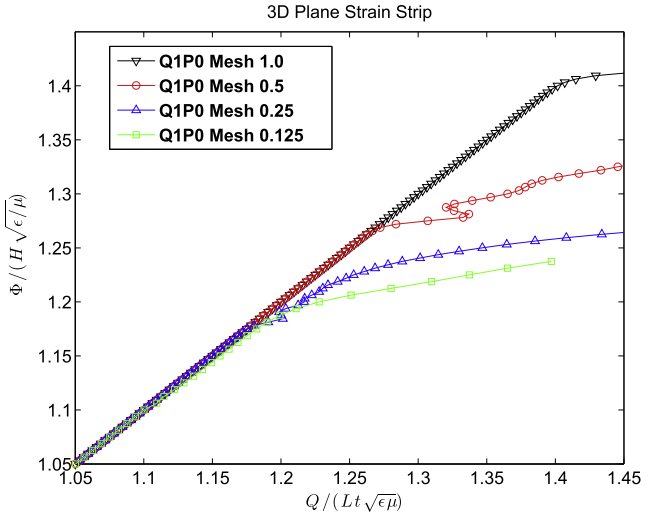

Fig. 6. Convergence of the normalized critical voltage Φ for electromechanical instability for the proposed Q1P0 element with increasing mesh density. $H = 4$ is the height of the film, Q is the charge at the top surface of the film, $L = 100$ is the length of the film, $t = 1$ is the thickness of the film, $\epsilon = 1.0$ is the dielectric constant, Φ is the voltage, and $\mu = 1$ is the shear modulus.

Because the Q1P0 result differs from the observed theoretical and experimental value for the critical voltage for a coarse FEM mesh, we study the convergence of the proposed Q1P0 formulation towards the experimental result with increasing FEM mesh density. We show this result in Fig. (6), where the normalized voltage-charge curves are shown for three different mesh densities of the Q1P0 formulation. As previously discussed in Fig. (5), for the coarsest element spacing of 1.0, $\tilde{\mathbf{E}}_c \approx 1.41$. However, for the finer element spacings of 0.5, 0.25 and 0.125, $\tilde{\mathbf{E}}_c \approx 1.27$, 1.18 and 1.10, respectively, which demonstrates that the Q1P0 formulation converges towards the analytic solution of $\tilde{\mathbf{E}}_c = 1.0$ with increasing mesh density. We also note that the mesh size of 0.125 constitutes an effective upper bound on mesh density as the simulation with this mesh size required nearly one month to complete. It should also be emphasized from a computational efficiency viewpoint that mesh refinement is considerably easier and less expensive using standard linear 8-node hexahedral elements than using the quadratic 27-node elements.

These results clearly demonstrate that if volumetric locking effects are not eliminated in the FEM modeling of DEs, artificially high predictions for critical applied voltages will result due to the fact that the deformation of standard FEs is artificially low for incompressible media.

6. Conclusions

We have presented a finite element formulation for dielectric elastomers that significantly alleviates the issue of volumetric locking. The formulation is novel in that it extends the seminal Q1P0 work of Simo et al. [1] to the coupled electromechanical domain. Numerical results were presented that demonstrate the ability of the proposed electromechanical Q1P0 formulation to capture, as compared to the experimental work of Wang et al. [2], both the critical electric field that is needed to cause creasing instabilities in constrained dielectric elastomer films, as well as the spacing between the creases.

Acknowledgements

HSP acknowledges support from the Mechanical Engineering Department at Boston University, and NSF grant CMMI-1036460. X.Z. and Q. W. acknowledge support from the NSF (CMMI-1253495, CMMI-1200515, and DMR-1121107).

References

[1] J.C. Simo, R.L. Taylor, K.S. Pister, Variational and projection methods for the volume constraint in finite deformation elasto-plasticity, Comput. Methods Appl. Mech. Engrg. 51 (1985) 177–208.
[2] Q. Wang, L. Zhang, X. Zhao, Creasing to cratering instability in polymers under ultrahigh electric fields, Phys. Rev. Lett. 106 (2011) 118301.
[3] F. Carpi, S. Bauer, D.D. Rossi, Stretching dielectric elastomer performance, Science 330 (2010) 1759–1761.
[4] P. Brochu, Q. Pei, Advances in dielectric elastomers for actuators and artificial muscles, Macromol. Rapid Commun. 31 (2010) 10–36.
[5] E. Biddiss, T. Chau, Dielectric elastomers as actuators for upper limb prosthetics: challenges and opportunities, Med. Engrg. Phys. 30 (2008) 403–418.
[6] Y. Bar-Cohen, Biomimetics: mimicking and inspired-by biology, Proc. SPIE 5759 (2005) 1–8.
[7] T. Mirfakhrai, J.D.W. Madden, R.H. Baughman, Polymer artificial muscles, Mater. Today 10 (2007) 30–38.
[8] A. O'Halloran, F. O'Malley, P. McHugh, A review on dielectric elastomer actuators, technology, applications, and challenges, J. Appl. Phys. 104 (2008) 071101.
[9] X. Zhang, C.L.M. Wissler, B. Jaehne, G. Kovacs, Dielectric elastomers in actuator technology, Adv. Engrg. Mater. 7 (2005) 361–367.
[10] R.E. Pelrine, R.D. Kornbluh, J.P. Joseph, Electrostriction of polymer dielectrics with compliant electrodes as a means of actuation, Sens. Actuators A 64 (1998) 77–85.
[11] Q. Wang, M. Tahir, J. Zang, X. Zhao, Dynamic electrostatic lithography: multiscale on-demand patterning on large-area curved substrates, Adv. Mater. 24 (2012) 1947–1951.
[12] P. Shivapooja, Q. Wang, B. Orihuela, D. Rittschof, G.P. Lopez, X. Zhao, Bioinspired surfaces with dynamic topography for active control of biofouling, Adv. Mater. 25 (2013) 1430–1434.
[13] R. Pelrine, R. Kornbluh, Q. Pei, J. Joseph, High-speed electrically actuated elastomers with strain greater than 100%, Science 287 (2000) 836–839.
[14] J.W. Fox, N.C. Goulbourne, On the dynamic electromechanical loading of dielectric elastomer membranes, J. Mech. Phys. Solids 56 (2008) 2669–2686.
[15] C. Keplinger, M. Kaltenbrunner, N. Arnold, S. Bauer, Rontgen's electrode-free elastomer actuators without electromechanical pull-in instability, Proc. Natl. Acad. Sci. 107 (2010) 4505–4510.
[16] G. Kofod, P. Sommer-Larsen, R. Kornbluh, R. Pelrine, Actuation response of polyacrylate dielectric elastomers, J. Intel. Mater. Syst. Struct. 14 (2003) 787–793.
[17] G. Kofod, P. Sommer-Larsen, Silicone dielectric elastomer actuators: finite-elasticity model of actuation, Sens. Actuators A 122 (2005) 273–283.
[18] Q. Pei, R. Pelrine, M. Rosenthal, S. Stanford, H. Prahlad, R. Kornbluh, Recent progress on electroelastomer artificial muscles and their application for biomimetic robots, Proc. SPIE 5385 (2004) 41–50.
[19] J.-S. Plante, S. Dubowsky, Large-scale failure modes of dielectric elastomer actuators, Int. J. Solids Struct. 43 (2006) 7727–7751.
[20] J.-S. Plante, S. Dubowsky, On the performance mechanisms of dielectric elastomer actuators, Sens. Actuators A 137 (2007) 96–109.
[21] J.-S. Plante, S. Dubowsky, On the properties of dielectric elastomer actuators and their design implications, Smart Mater. Struct. 16 (2007) S227–S236.
[22] H.F. Schlaak, M. Jungmann, M. Matysek, P. Lotz, Novel multilayer electrostatic solid-state actuators with elastic dielectric, Proc. SPIE 5759 (2005) 121–133.
[23] M. Wissler, E. Mazza, Mechanical behavior of an acrylic elastomer used in dielectric elastomer actuators, Sens. Actuators A 134 (2007) 494–504.
[24] X.Q. Zhang, M. Wissler, B. Jaehne, R. Broennimann, G. Kovacs, Effects of crosslinking, prestrain and dielectric filler on the electromechanical response of a new silicone and comparison with acrylic elastomer, Proc. SPIE 5385 (2004) 78–86.
[25] S. Chiba, M. Waki, R. Kornbluh, R. Pelrine, Innovative power generators for energy harvesting using electroactive polymer artificial muscles, Proc. SPIE 6927 (2008) 692715.
[26] Z. Suo, X. Zhao, W.H. Greene, A nonlinear field theory of deformable dielectrics, J. Mech. Phys. Solids 56 (2008) 467–486.
[27] Z. Suo, Theory of dielectric elastomers, Acta Mech. Solida Sinica 23 (2010) 549–578.
[28] N.C. Goulbourne, E.M. Mockensturm, M.I. Frecker, A nonlinear model for dielectric elastomer membranes, J. Appl. Mech. 72 (2005) 899–906.
[29] A. Dorfmann, R.W. Ogden, Nonlinear electroelasticity, Acta Mech. 82 (2005) 99–127.
[30] A. Dorfmann, R.W. Ogden, Nonlinear electroelastic deformations, J. Elast. 174 (2006) 167–183.
[31] R.M. McMeeking, C.M. Landis, Electrostatic forces and stored energy for deformable dielectric materials, J. Appl. Mech. 72 (2005) 581–590.
[32] L. Patrick, K. Gabor, M. Silvain, Characterization of dielectric elastomer actuators based on a hyperelastic film model, Sens. Actuators A 135 (2007) 748–757.
[33] M. Wissler, E. Mazza, Modeling and simulation of dielectric elastomer actuators, Smart Mater. Struct. 14 (2005) 1396–1402.
[34] G.A. Maugin, Continuum mechanics of electromagnetic solids, North-Holland, Amsterdam, 1988.
[35] K. Bertoldi, M. Gei, Instabilities in multilayered soft dielectrics, J. Mech. Phys. Solids 59 (2011) 18–42.
[36] W. Hong, Modeling viscoelastic dielectrics, J. Mech. Phys. Solids 59 (2011) 637–650.
[37] A. Dorfmann, R.W. Ogden, Nonlinear electroelastostatics: incremental equations and stability, Int. J. Engrg. Sci. 48 (2010) 1–14.
[38] X. Zhao, W. Hong, Z. Suo, Electromechanical hysteresis and coexistent states in dielectric elastomers, Phys. Rev. B 76 (2007) 134113.
[39] M. Ottenio, M. Destrade, R.W. Ogden, Incremental magnetoelastic deformations, with application to surface instability, J. Elast. 90 (2008) 19–42.
[40] Q. Wang, M. Tahir, L. Zhang, X. Zhao, Electro-creasing instability in deformed polymers: experiment and theory, Soft Matter 7 (2011) 6583–6589.
[41] X. Zhao, Z. Suo, Method to analyze programmable deformation of dielectric elastomers, Appl. Phys. Lett. 93 (2008) 251902.
[42] D.K. Vu, P. Steinmann, G. Possart, Numerical modelling of non-linear electroelasticity, Int. J. Numer. Methods Engrg. 70 (2007) 685–704.
[43] J. Zhou, W. Hong, X. Zhao, Z. Zhang, Z. Suo, Propagation of instability in dielectric elastomers, Int. J. Solids Struct. 45 (2008) 3739–3750.
[44] B. O'Brien, T. McKay, E. Calius, S. Xie, I. Anderson, Finite element modelling of dielectric elastomer minimum energy structures, Appl. Phys. A - Mater. Sci. Process. 94 (2009) 507–514.
[45] M. Wissler, E. Mazza, Electromechanical coupling in dielectric elastomer actuators, Sens. Actuators A 138 (2007) 384–393.
[46] H.S. Park, T.D. Nguyen, Viscoelastic effects on electromechanical instabilities in dielectric elastomers, Soft Matter 9 (2013) 1031–1042.
[47] K.A. Khan, H. Wafai, T.E. Sayed, A variational constitutive framework for the nonlinear viscoelastic response of a dielectric elastomer, Comput. Mech. (2012), http://dx.doi.org/10.1007/s00466-012-0815-6.

[48] M. Wissler, E. Mazza, Modeling of a pre-strained circular actuator made of dielectric elastomers, Sens. Actuators A 120 (2005) 184–192.
[49] S. Skatulla, C. Sansour, A. Arockiarajann, A multiplicative approach for nonlinear elasto-elasticity, Comput. Methods Appl. Mech. Engrg. 245-246 (2012) 245–253.
[50] H.S. Park, Z. Suo, J. Zhou, P.A. Klein, A dynamic finite element method for inhomogeneous deformation and electromechanical instability of dielectric elastomer transducers, Int. J. Solids Struct. 49 (2012) 2187–2194.
[51] Z.P. Bazant, T.B. Belytschko, Wave propagation in a strain-softening bar: exact solution, J. Engrg. Mech. 111 (1985) 381–385.
[52] T. Belytschko, W.K. Liu, B. Moran, Nonlinear Finite Elements for Continua and Structures, John Wiley and Sons, 2002.
[53] E. Schaffer, T. Thurn-Albrecht, T.P. Russell, U. Steiner, Electrically induced structure formation and pattern transfer, Nature 403 (2000) 874–877.
[54] X. Zhao, Z. Suo, Method to analyze electromechanical instability of dielectric elastomers, Appl. Phys. Lett. 91 (2007) 061921.
[55] J. Huang, T. Li, C.C. Foo, J. Zhu, D.R. Clarke, Z. Suo, Giant, voltage-actuated deformation of a dielectric elastomer under dead load, Appl. Phys. Lett. 100 (2012) 041911.
[56] C.C. Foo, S. Cai, S.J.A. Koh, S. Bauer, Z. Suo, Model of dissipative dielectric elastomers, J. Appl. Phys. 111 (2012) 034102.
[57] E.M. Arruda, M.C. Boyce, A three-dimensional constitutive model for the large stretch behavior of rubber elastic materials, J. Mech. Phys. Solids 41 (1993) 389–412.
[58] T.J.R. Hughes, The Finite Element Method: Linear Static and Dynamic Finite Element Analysis, Prentice-Hall, 1987.
[59] G.A. Holzapfel, Structural and numerical models for the Viscoelastic response of arterial walls with residual stresses, Springer, pp. 109–184.
[60] C. Miehe, Numerical computation of algorithmic (consistent) tangent moduli in large-strain computational inelasticity, Comput. Methods Appl. Mech. Engrg. 134 (1996) 223–240.
[61] Tahoe, 2011. <http://sourceforge.net/projects/tahoe/>.
[62] Q. Wang, Z. Suo, X. Zhao, Bursting drops in solid dielectrics caused by high voltages, Nat. Commun. 3 (2012) 1157.